MAVEN and the total electron content of the Martian ionosphere

Michael Mendillo, Clara Narvaez, Marissa F. Vogt, Majd Mayyasi, Paul Mahaffy, Mehdi Benna, Laila Anderson, Bruce Campbell, Frantisek Němec, Ying Juan Ma, et al.

AGU PUBLICATIONS

JGR

Journal of Geophysical Research: Space Physics

RESEARCH ARTICLE
10.1002/2016JA023474

Special Section:
Major Results From the MAVEN Mission to Mars

MAVEN and the total electron content of the Martian ionosphere

Michael Mendillo[1], Clara Narvaez[1], Marissa F. Vogt[1], Majd Mayyasi[1], Paul Mahaffy[2], Mehdi Benna[2], Laila Andersson[3], Bruce Campbell[4], Frantisek Němec[5], Ying Juan Ma[6], Jean-Yves Chaufray[7], François Leblanc[7], Francisco Gonzalez-Galindo[8], Miguel Ángel Lopez-Valverde[8], François Forget[9], and Bruce Jakosky[3]

[1]Center for Space Physics, Boston University, Boston, Massachusetts, USA, [2]NASA Goddard Space Flight Center, Greenbelt, Maryland, USA, [3]LASP, University of Colorado Boulder, Boulder, Colorado, USA, [4]Smithsonian Institution, Washington, DC, USA, [5]Faculty of Mathematics and Physics, Charles University, Prague, Czech Republic, [6]Department of Earth and Planetary Sciences, University of California, Los Angeles, California, USA, [7]LATMOS/IPSL, UPMC, Université Paris 06, Sorbonne Universités, UVSQ, CNRS, Paris, France, [8]Instituto de Astrofisica de Andalucia, CSIC, Granada, Spain, [9]Laboratoire de Météorologie, Dynamique, CNRS, Paris, France

Key Points:
- MAVEN's in situ plasma observations used to obtain topside ionosphere's total electron content validated by models and independent data
- MAVEN's April 2015 Deep-Dip-#2 campaign provided clear evidence of a <TE> topside depletion event
- A single ionopause contraction episode matched ambient plasma loss rates of ~3×10^{24} ions/s

Correspondence to:
C. Narvaez,
cnarvaez@bu.edu

Citation:
Mendillo, M., et al. (2017), MAVEN and the total electron content of the Martian ionosphere, *J. Geophys. Res. Space Physics*, *122*, 3526-3537, doi:10.1002/2016JA023474.

Received 15 SEP 2016
Accepted 14 FEB 2017
Accepted article online 18 FEB 2017
Published online 7 MAR 2017

Abstract Model studies of the ionosphere of Mars under daytime conditions reveal that for solar zenith angles of 0°–40°, the shapes and magnitudes of the electron density profiles $N_e(h)$ change by only small amounts. This suggests that midday observations made by MAVEN instruments along slanted orbit segments can be used to represent vertical profiles. The total electron content (TEC), defined as the height integral of $N_e(h)$, is a measure of the cold plasma reservoir of the Martian ionosphere. During MAVEN's Deep-Dip-#2 campaign of April 2015, observations of total ion density by Neutral Gas and Ion Mass Spectrometer and electron density by Langmuir Probe and Waves from periapse (~130 km) to 400 km were used to form $<\text{TEC}>_{\text{topside}}$—validated by independent diagnostics and models. Orbit-by-orbit changes in topside TEC were then used to assess the magnitudes of plasma escape associated with both large and small changes in the topside slope of $N_e(h)$—called an "ionopause episode." The TEC changes due to these episodes, generalized to a global change, resulted in an escape flux of ~$3–6 \times 10^{24}$ ions/s, an escape rate consistent with prior observation by Phobos-2, Mars Express, and MAVEN's own in situ studies.

1. Introduction

The MAVEN mission is currently investigating the modes of escape of neutral and ionized gases from Mars with the goal of assessing the long-term history of atmospheric loss [*Jakosky*, 2015]. The cold plasma component of atmospheric escape comes from the Martian ionosphere, a region spanning the altitude range of ~80–400 km. The loss mechanisms are upward diffusion and horizontal transport to altitudes where solar wind "pickup" or "ionospheric stripping" processes remove plasma from the system. MAVEN's orbit does not allow in situ plasma observations to sample the full vertical profile of electron density, $N_e(h)$. Yet it routinely measures the ~150–400 km altitude domain, and during occasional "deep dip" orbital maneuvers, observations extend to ~130 km. In this study, we explore ways to use MAVEN's broad sampling capabilities of the Martian ionosphere to make quantitative estimates of the reservoir of thermal plasma capable of escape.

Many past studies [see *Haider et al.*, 2011] have shown that the ionosphere of Mars can be divided into fairly distinct height regimes: At altitudes between ~80 and ~170 km, the solar produced plasma is embedded in a dense neutral atmosphere, and the time rates of change due to chemistry are faster than transport effects (time constants given in Figure 16 in *Mendillo et al.*, 2011). Within this photo-chemical-equilibrium domain, there are two ionospheric layers—a low-altitude M_1 layer with maximum electron density N_mM_1 at ~110 km and a more robust M_2 layer above it having a maximum density denoted N_mM_2 at height $h_{\max}$ ~125–135 km. The so-called bottomside ionosphere, defined as $h < h_{\max}$, has no direct involvement in the loss process. The regime of importance for escape is in the topside ionosphere between heights ~170 km to ~400 km where in situ chemistry competes with plasma dynamics.

MAVEN samples ionospheric densities below 400 km along segments of an elliptical orbit— traversing a broad range of horizontal space with strong variations of solar zenith angle (SZA). For example, on a "deep-dip" day to be analyzed in detail below (orbit #1082, inbound, on 21 April 2015), MAVEN crossed 400 km at UT = 17:04, latitude = −42°, longitude = 72°, with SZA = 33°. The periapse height of ~132 km was reached at UT = 17:14, with latitude = −5.6°, longitude = 82.75°, and SZA = 8°. MAVEN's vertical sampling of

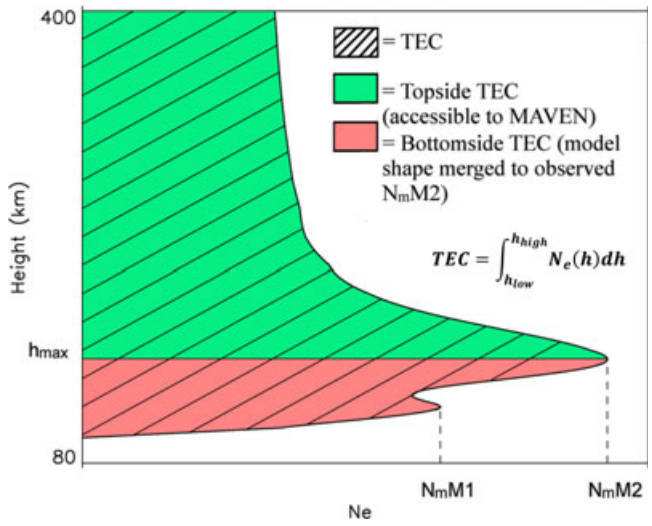

Figure 1. A schematic representation of the Martian ionosphere depicting the full altitude range for total electron content (TEC), together with components above $(TEC)_{topside}$ and below $(TEC)_{bottomside}$ the height of maximum electron density (h_{max}). MAVEN in situ observations occur within the topside portions indicated by green shading.

the Martian ionosphere thus spanned nearly 3000 km of horizontal space, with SZAs changing by ~25°. A true *vertical* sampling of the ionosphere between 132 and 400 km would, of course, give $N_e(h)$ at single values of latitude, longitude, and SZA. Is it possible to use MAVEN in situ plasma observations to arrive at an equivalent vertical sampling of the Martian topside ionosphere—the reservoir of plasma capable of escape?

2. Total Electron Content

The total electron content (TEC) of the Martian ionosphere is defined as the integral with height of the planet's electron density profile, $N_e(h)$,

$$\mathrm{TEC} = \int N_e(h)dh \qquad (1)$$

Past observational and modeling studies can be used to select the altitude limits of the integral. With a consensus choice for h_{low} being 80 km, the h_{high} to use depends on solar wind conditions. When the solar wind is not particularly strong, ~400 km becomes the maximum altitude of relevance [*Fox*, 2004], and that is the one we will adopt in this study. During periods of enhanced solar wind pressure, however, the ionosphere can terminate rather abruptly at altitudes of ≤300 km—a signature called the "ionopause" [*Duru et al.*, 2009; *Vogt et al.*, 2015, and references therein]. For such cases, ionospheric depletions at high altitudes have clearly occurred and the remaining TEC is reduced in absolute magnitude. Plasma escape is thus fundamentally involved with the structure of the topside ionosphere and its contributions to the TEC integral. This is precisely the altitude domain covered extensively by the MAVEN spacecraft.

Figure 1 offers a schematic representation of the altitude components of TEC as a guide to the approach to be used. TEC values are typically expressed in MKS units as column contents per square meter, with one TEC unit (TECU) equal to $10^{15}\,e^{-}/m^{-2}$.

3. TEC From Models of the Martian Ionosphere

3.1. Climatological Modeling

A first attempt to create a data-based model for the topside portion of the Martian ionosphere is described in *Němec et al.* [2011, 2016]. Using radio soundings from the Mars Advanced Radar for Subsurface and Ionospheric Sounding (MARSIS) on board the Mars Express (MEX) satellite, vertical electron density observations from h_{max} to the satellite height were cast into a retrievable format based on solar activity, SZA, season, and crustal magnetic field morphologies. Model runs for the conditions found on 21 April 2015 during MAVEN's Deep-Dip-#2 campaign ($F_{10.7} = 51$, $\mathbf{B} = 14.16$ nT, Sun-Mars distance = 1.48 AU), for SZA samples between 5° and 35°, are shown in Figure 2. Since our initial interests are with the shapes of $N_e(h)$ in the topside ionosphere, the *Němec et al.* [2016] profiles have been normalized to unity by using their N_mM_2 values. We will discuss absolute values below.

3.2. Semi-Empirical Modeling

Using the maximum electron density values (N_mM_2) from MARSIS spanning the period of 2005 to 2012, a Mars Initial Reference Ionosphere (MIRI) model was created by fitting 112,000 data points to the photo-chemical-equilibrium equation relating N_mM_2 to SZA and the solar flux index $F_{10.7}$ [*Mendillo et al.*, 2013a]. To achieve full $N_e(h)$ profiles, the MIRI N_mM_2 values were then used to calibrate the normalized shapes of $N_e(h)$ profiles versus SZA obtained from the Boston university theoretical model [*Martinis et al.*, 2003; *Mendillo et al.*, 2011; *Mayyasi*

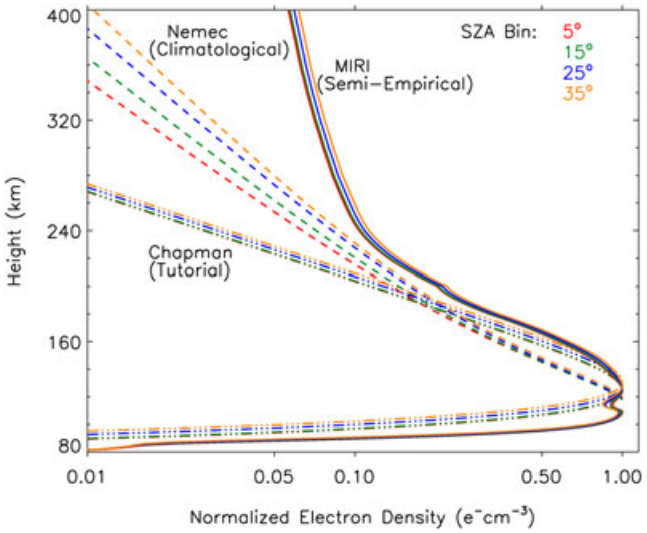

Figure 2. Comparison of three 1-D models representing the Martian ionosphere under conditions of midday to midafternoon solar zenith angles. In all cases, the profiles have been normalized to unity at the height of their maximum electron density. The Mars Initial Reference Ionosphere (MIRI) curves use theoretical profiles calibrated by MIRI's N_{max}. The climatological profiles are derived entirely from observations of the topside ionosphere, with their bottomside shapes coming from MIRI's theoretical curves. The Chapman profiles use a 14 km neutral scale height to achieve a best match to the MIRI shapes at h_{max} (see text for discussion and references).

and Mendillo, 2015]. The resultant MIRI-mark-2 is described in *Mendillo et al.* [2015]. Figure 2 shows the normalized theoretical profiles that are the basis of MIRI-mark-2 for the same 5°–35° range of SZAs. The topside ionosphere morphologies are clearly different between the purely theoretical and fully climatological models. Note also that the bottomside portions of the MIRI $N_e(h)$ profiles include the M_1 and M_2 layers not available from the Němec et al. model.

3.3. Tutorial Model

The first mathematical description of an ionosphere was presented in the classic studies by Sydney Chapman in the early 1930s. While many simplifying assumptions were made, the impact of his innovative approach (coupled to the high personal regard for Chapman as a scientist) led to any observational departures from "Chapman Theory" to be called *Anomalies* (diurnal, seasonal, and equatorial), as described in *Ratcliffe* [1960] and *Rishbeth and Garriot* [1969]. The anomalies, of course, were not observational errors but naturally occurring effects not possible of simulation using the restrictive set of conditions proposed by Chapman. While Chapman Theory remains good tutorial material for the classroom, it has been many decades since it was used as a research tool in terrestrial ionospheric research. Yet its legacy is still prominent in less well-documented ionospheres, including the Martian case (see historical review in *Withers* [2009]). For this reason, Figure 2 also contains a set of Chapman profiles to complete the possible ways to represent the Martian ionosphere under low-SZA conditions.

Figure 2 summarizes an important aspect of Martian aeronomy—diverse models exhibit dramatic differences in ways to represent the topside ionosphere of Mars. The theoretical curves used in MIRI are from a one-dimensional model that adds vertical plasma diffusion to photo-chemistry. The topside gradient shows a transition in plasma scale height from heavy to lighter ions near ~240 km. The climatological model portrays the overall observed ionospheric characteristics arising from all possible chemical, transport, and escape processes. Its topside gradient has a nearly constant plasma scale height above the peak. Chapman profiles describe a layer with the most simple photo-chemistry and no plasma transport of any kind, with its topside gradient following that of the neutral scale height. The first conclusion to be drawn from Figure 2 is that the Němec et al. climatologies differ from the theoretical profiles obtained by using multispecies chemistry and vertical diffusion to shapes that look like Chapman profiles. This is due to transport effects that enhance the topside gradient—an effect that should not be confused with validation of Chapman Theory for $h > h_{max}$. The second conclusion from Figure 2, and the one of more relevance to this study, is that regardless of the model used all of the $N_e(h)$ shapes are very similar for midday conditions. This tells us that "a direct integration of MAVEN observations along a highly slanted trajectory through the ionosphere will yield credible values of topside TEC for midday ionospheric conditions at Mars." We now test this by using MAVEN data, independent TEC observations, and state-of-the-art models.

4. MAVEN Observations

MAVEN's Neutral Gas and Ion Mass Spectrometer (NGIMS) provides data on the thermal ionic species along an orbit [*Mahaffy et al.*, 2014]. The Langmuir Probe and Waves (LPW) instrument provides observations of electron density [*Andersson et al.*, 2015; *Ergun et al.*, 2015]. Under the well-justified assumption of charge neutrality for a

cold ionospheric plasma, the sum of NGIMS ions and the LPW electron density should agree. The instruments are calibrated independently, however, and small differences are seen (as will be shown below).

MAVEN conducted a six-day orbital "Deep-Dip" campaign (27 orbits between 17 and 22 April 2015) when the periapse point was lowered to ~132 km within the noontime sector (sampling the same trans-equatorial latitudes below 400 km, but at various longitudes). Under such conditions, NGIMS and LPW observations often showed a slight reversal in gradient (i.e., crossing below the $dN_e/dh = 0$ point), and for these cases we used the values at the altitudes of maximum density (h_{max}) as N_{max}. For a few other cases, MAVEN did not go below h_{max}, and for these we used the lowest altitude as h_{max} (probably within ±1–2 km of the actual h_{max}, as judged by the previous cases). The fact that the sum of ions from NGIMS does not always equal the electron density from LWP is an observational ambiguity that is larger than the uncertainties of where h_{max} occurs. Fortunately, this does not have a serious effect upon the topside TEC values we will discuss since we process data from each instrument separately.

Figure 3 (top middle) shows the Deep-Dip-#2 inbound and outbound trajectories as a function of altitude and solar zenith angle. The ionospheric plasma densities measured versus height appear to the left (inbound) and right (outbound). The NGIMS total-ion observations are plotted by using black dots, and the LPW electron density data are shown by using orange squares. There are twice as many LPW data points because NGIMS has a 50% duty cycle between ion and neutral gas measurements for inbound-outbound orbits.

Figure 3 (bottom row) give the averages of the upper panels. NGIMS values are somewhat lower in absolute value than LPW data at lower altitudes, with that trend reversing at higher altitudes. The NGIMS and LPW average patterns in Figure 3 (bottom row) differ by amounts within the statistical uncertainties of the patterns above (see the Acknowledgments section for versions used). Using the conclusion from Figure 2 that midday samplings of the ionosphere will find mild spatial gradients about the subsolar point, integration of the MAVEN data offers a representative measure of the topside ionosphere's contribution to a TEC value. To obtain a MAVEN overall sample average, we integrated the instrument average results (NGIMS and LPW, inbound and outbound) using two topside heights (400 km and 270 km). These altitude limits are appropriate for observations of TEC made by the MARSIS instrument on Mars Express (MEX) and the Shallow Radar (SHARAD) instrument on Mars Reconnaissance Orbiter (MRO), to be discussed below. The resultant numerical values are (a) MAVEN $< \text{TEC} >_{\text{topside}}$ to 400 km = 5.1 TECU and (b) MAVEN $< \text{TEC} >_{\text{topside}}$ to 270 km = 4.9 TECU. Thus, 98% of the topside TEC resides below 270 km.

5. Observations of TEC at Mars

5.1. Previous TEC Observations at Mars

The integration of electron density profiles obtained by the radio occultation method [*Hinson et al.*, 1999] was first used to form TEC values in the study by *Mendillo et al.* [2004]. Using 209 profiles from December 1998 to December 2000, the computed TEC values for near-terminator conditions had magnitudes in a narrow range of values (4.4 ± 0.4 TECU). A far more significant advance in the use of TEC data for ionospheric research at Mars came with the development of satellite-based radars designed to search for subsurface signatures of water. On the Mars Express (MEX) satellite, the Mars Advanced Radar for Subsurface and Ionospheric Sounding (MARSIS) instrument [*Picardi et al.*, 2004, 2005; *Jordan et al.*, 2009] measures radio wave group path delay to and from the surface, which is derived from the total electron content of the Martian ionosphere [*Safaeinili et al.*, 2003, 2007; *Picardi et al.*, 2005; *Mouginot et al.*, 2008; *Zhang et al.*, 2009; *Cartacci et al.*, 2013; *Sanchez-Cano et al.*, 2015]. The initial set of MARSIS observations yielded approximately 1.4 million TEC values over the course of a full Martian year (from 19 June 2005 to 30 September 2007.). These data have been used to investigate TEC patterns due to variations in solar flux and solar zenith angle [*Safaeinili et al.*, 2007; *Lillis et al.*, 2010; *Cartacci et al.*, 2013], as well as to document ionospheric variability on global and regional spatial scales [*Mendillo et al.*, 2013b].

As part of the MIRI effort, a TEC module was developed from MARSIS data to predict daytime TEC as a function of SZA and the solar radio flux index ($F_{10.7}$), yielding the following functional dependence at Mars' average distance from the Sun (1.54 AU):

$$\text{TEC}\left(e^{-}/m^{2}\right) = 1.2 \times 10^{15} \times \sqrt{\cos(\text{SZA}) \times \text{RF}} \tag{2}$$

$$\text{with RF} = \frac{F10.7_{(\text{day})} + <F10.7>_{(81\ \text{day})}}{2} \tag{3}$$

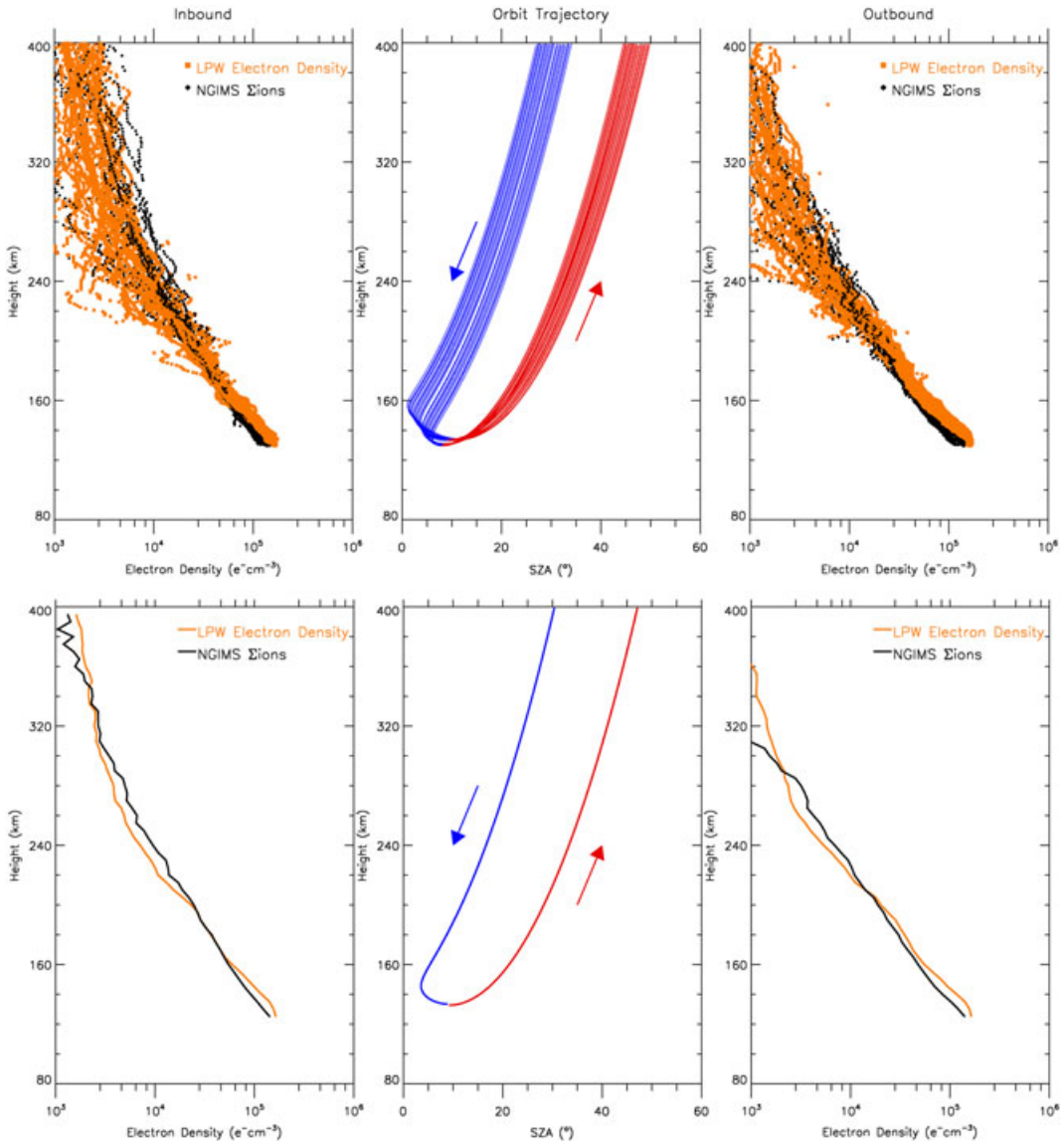

Figure 3. MAVEN observations by NGIMS (total ions, black dots) and LPW (electron density, orange squares) during the 17–23 April 2015 Deep-Dip campaign. (top row) Inbound data (left) and outbound data (right). (middle) The MAVEN trajectories depicted versus height and solar zenith angles, with blue for inbound and red for outbound orbit segments. (bottom) The averages of Figure 3 (top row).

The $F_{10.7}$ index (observed at Earth) to apply at Mars is obtained by using the "rotated Sun" method to account for orbital longitude differences between Earth and Mars. Once the TEC at 1.524 AU is obtained, it is adjusted by a 1/distance orbital distance correction associated with photo-chemical-equilibrium processes [*Mendillo et al.*, 2015].

For the 17–22 April 2015 period, Mars was at an orbital distance of 1.48 AU, and the solar radio flux parameter in equation (3) was essentially constant with $<RF>=51$ units at 1.524 AU. Using $<SZA \geq 20°$ for heights 80–400 km, the resultant TEC value from equation (2) is 8.8 TECU. As anticipated, this is several TECU higher than the MAVEN value computed above because MARSIS measures the full TEC, i.e., both topside and bottomside components.

5.2. Same-Day TEC Observations at Mars: 21 April 2015

The Mars Reconnaissance Orbiter (MRO) spacecraft is in a circular orbit at approximately 270 km altitude. Its Shallow Radar (SHARAD), as with MARSIS on MEX, yields TEC values as a by-product of the postprocessing

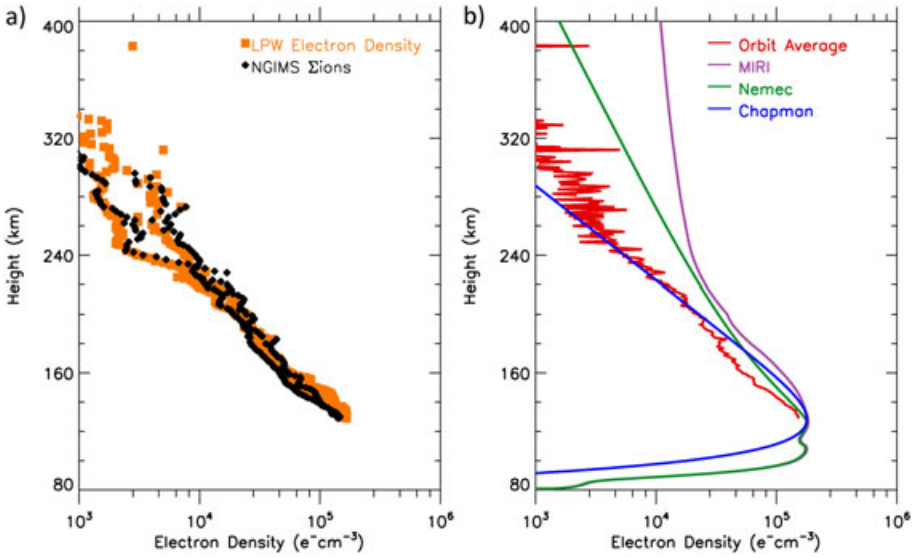

Figure 4. (a) Observations by NGIMS and LPW on 21 April 2015 during inbound orbit #1082 (17:04:09–17:13:59 UT) and outbound orbit #1083 (17:14:03 – 17:23:41 UT). (b) Average of NGIMS and LPW results shown in comparison to the three models given in Figure 2 for 21 April 2015 conditions (see text). The average N_{max} from LPW and NGIMS is 15.3×10^4 e$^-$ cm^{-3}. The average N_{max} from MIRI and Němec is 18.1×10^4 e$^-$ cm^{-3}.

required to minimize ionospheric effects on range delay and image distortion of subsurface targets. The SHARAD instrument is described by *Seu et al.* [2007], with ionospheric retrieval methods presented by *Campbell et al.* [2011, 2013, 2014]. Comparisons of SHARAD and MARSIS are presented in *Campbell and Watters* [2016]. Due to MRO's circular orbit, SHARAD's TEC observations have a fixed upper boundary for the integral of $N_e(h)$ with height. As will be shown below, virtually all of the TEC of the Martian ionosphere is captured in data spanning ~80 to ~270 km, and thus, same-day TECs from SHARAD are highly relevant to our study.

During MAVEN's 17–22 April 2015 Deep-Dip campaign, MRO/SHARAD made TEC measurements only on 21 April 2015—with observations within the latitude band of 4.5°–8.5°N, at longitude = 67° and SZA = 39°. Of the five MAVEN orbits on that day, the closest ones were #1082 and #1083 with an average SZA = 23° at latitude 5°S and longitude 83°. The SHARAD TEC value is 8.8 TECU, consistent with the MIRI estimate given above.

Figure 4a shows MAVEN in situ plasma observations from LPW and NGIMS for the specific case study of 21 April 2015. The two-orbit average of MAVEN's NGIMS and LPW topside data relate to $<$SZA$>$ = 20° and is shown in Figure 4b by the red line. Also in the graph are three curves from the models depicted in Figure 2. The MIRI results are given by the solid purple line, the Němec et al. climatology model by the solid green line (with the bottomside portion taken from the theoretical curve for SZA = 25° in Figure 2), and Chapman results, calibrated by the mean of the MIRI and Němec predictions, by the blue line. The four profiles can be integrated to yield TEC results. Table 1 summarizes the several ways to do so: (a) TEC from 80 to 400 km, (b) topside content ($h > h_{max}$), (c) bottomside content ($h < h_{max}$), and (d) TEC from 80 to 270 km (for SHARAD comparisons).

Several interesting results appear in Table 1: (1) The contributions of electron densities above 270 km amount to only ≤5% of the TEC integral up to 400 km, with the exception of MIRI's ~10%. (2) The contribution of electron densities from the bottomside ionosphere are a significant fraction of the overall TEC. This is due to the small-altitude extent of the topside Martian ionosphere (e.g., TEC computations at Earth have h_{max} at ~300 km and the upper height of the TEC integral at ~2000 km). (3) The least sophisticated model (Chapman Theory) gives the best numerical match to the observed 8.8 TECU valued observed by SHARAD (line (d) in Table 1). A possible reason for this was given above, namely, that horizontal transport has the effect of removing plasma from the topside ionosphere [*Withers et al.*, 2012; *Cui et al.*, 2015]—accounting for the differences between the MIRI $N_e(h)$ profiles from 1-D theory and the Němec et al. topside model from observations. Thus, for this period, more horizontal transport occurred for these subsolar conditions than

Table 1. Comparison of MAVEN Observations With Model Results for 21 April 2015[a]

		NGIMS		LPW		Němec et al.		MIRI		Chapman	
		TECU[b]	%	TECU[b]	%	TECU[b]	%	TECU[b]	%	TECU[b]	%
(a)	80–400 km	9.2	100.0	10.1	100.0	13.3	100.0	16.6	100.0	10.3	100.0
(b)	Topside	4.8	52.2	5.1	49.9	8.1	61.0	11.2	67.6	7.2	69.8
(c)	Bottomside	4.4	47.8	5.1	50.1	5.2	39.0	5.4	32.4	3.1	30.2
(d)	80–270 km	9.1	98.8	10.0	98.3	12.7	95.5	14.8	89.6	10.3	99.5

[a]NGIMS, LPW, and *Němec et al.* [2016] results come from observations above h_{max}; their bottomside $N_e(h)$ values were formed by using the theoretical model's profile shape for SZA = 25° (Figure 2) calibrated by their individual N_mM_2 values.
[b]1 TEC unit (TECU) = 10^{15} e^-/m^{-2}.

were captured in the climatological results from *Němec et al.* [2016]. Alternately, solar wind-induced magnetic fields near noon could inhibit vertical transport, also resulting in changes of topside $N_e(h)$ profiles.

5.3. Same-Day Modeling of TEC at Mars: 21 April 2015

As a further validation of the constancy assumed for TEC throughout the midday period, simulations for the average conditions encountered during MAVEN's Deep-Dip-#2 campaign of April 2015 were obtained from three independent groups. These are (1) the theoretical 1-D fluid model used at Boston University for MIRI's $N_e(h)$ profile shapes [*Mayyasi and Mendillo*, 2015], (2) the MHD global model from University of California, Los Angeles (UCLA) described in *Ma et al.* [2004], and (3) the 3D Martian general circulation model from the Laboratoire de Météorlogie Dynamique [*Forget et al.*, 1999; *Gonzalez-Galindo et al.*, 2013]. This version differs from the one used to generate the Martian Climate Database by including ion dynamics [*Chaufray et al.*, 2014]. All three models predicted comparable values of maximum electron density (N_mM_2) consistent with the NGIMS and LPW observations shown in Figures 3 and 4. For total electron content, Figure 5 gives the diurnal patterns as portrayed by hourly values from all three models. There is an impressive consistency in their TEC values (8–10 TEC units) for several hours spanning local noon. While some variability occurred in the shapes of their altitude distributions of electron density, the integrals of their $N_e(h)$ profiles with height averaged out such differences. This emphasizes one of the most useful aspects of TEC-based studies—changes in TEC relate to real differences in plasma content, not merely to vertical redistributions of the existing plasma.

The minor differences in absolute values of TEC during daytime are due mainly to the different altitude ranges used in the three simulations: Boston University (BU) (80–400 km), UCLA (100–400 km), and Laboratoire Atmosphères, Milieux, Observations Spatiales (pressure levels relating to $h <$ ~250 km). In addition, the M_1 layer produced by soft X-rays is not included in the two global models. Finally, as can be seen, there are major inconsistencies in nighttime values between the three models, but these have no impact on the daytime patterns discussed here. They will be investigated in a follow-up study.

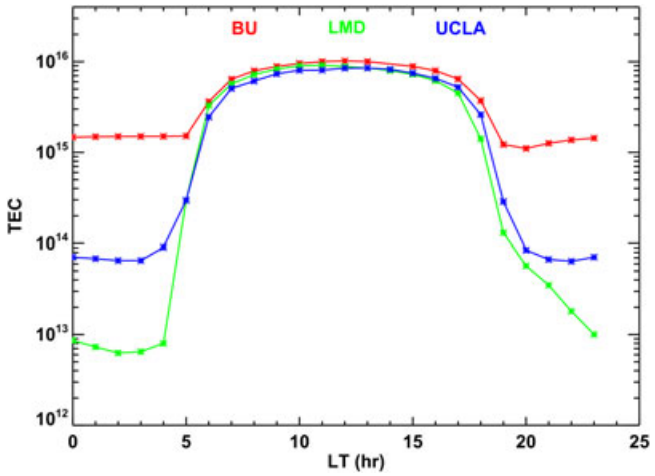

Figure 5. The diurnal patterns of total electron content (e^-/m^2) from three models run for conditions of 21 April 2015. The Boston University (BU); University of California, Los Angeles (UCLA); and the Laboratoire de Météorlogie Dynamique (LMD).

5.4. Day-to-Day Changes in TEC

We have presented several studies to demonstrate that the integrals of MAVEN's observations of both total ion density from NGIMS and electron density from LPW—from 400 km down to periapse height (~h_{max})—can be used as reliable indicators of plasma content of Mars' topside ionosphere. We now examine the

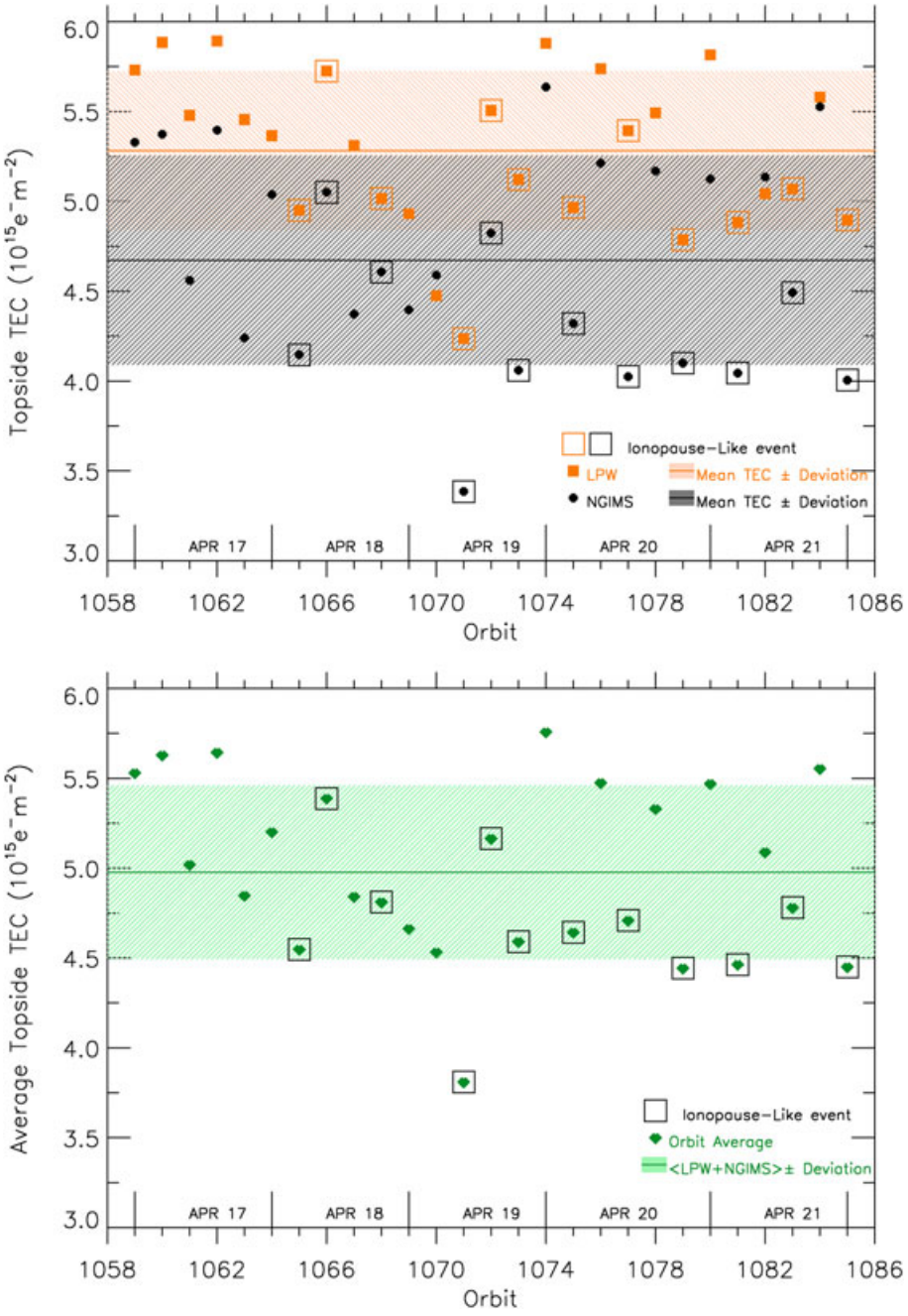

Figure 6. Topside total electron content values obtained by integration of the NGIMS and LPW observations from MAVEN's Deep-Dip-#2 campaign of April 2015. (top) Orbit-by-orbit values of $<TEC>_{topside}$ are shown by using color-coding for each instrument, with average values given by the solid lines and 1σ variability by the shadings. (bottom) Averages of NGIMS and LPW values from Figure 6 (top) to yield MAVEN-average $<TEC>_{topside}$ observations. The TEC values associated with ionopause events are indicated by points within squares.

pattern of daily changes in the magnitudes of $(TEC)_{topside}$ to assess the variability of Mars' topside cold plasma reservoir. Figure 6 gives orbit-by-orbit values of topside TEC from both instruments. We have used the half of the LPW data set that coincides in space and time with the NGIMS observations at periapse. In Figure 6 (top), the LPW and NGIMS observations are shown by using orange and black symbols, respectively, with the solid lines giving their average values, and with shadings to portray 1-sigma variabilities. The first item to notice is that calibration differences between the two instruments can be seen in the mean values: $<TEC>_{LPW} = 5.28 \pm 0.44$ and $<TEC>_{NGIMS} = 4.67 \pm 0.58$ TECU, showing that

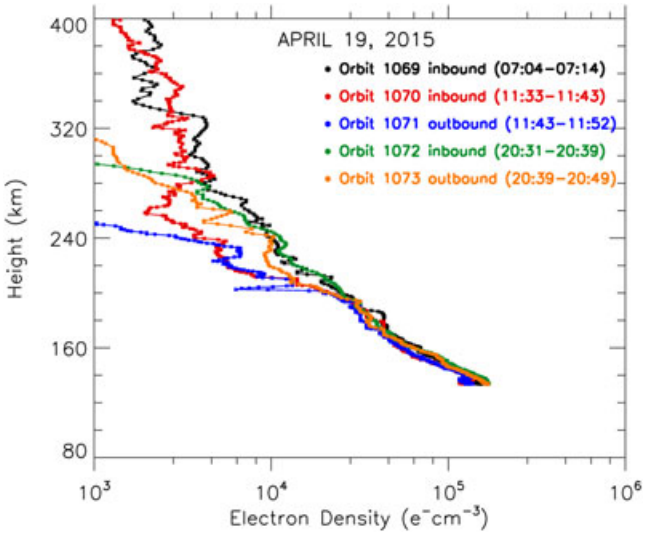

Figure 7. Topside $N_e(h)$ observations from LPW on 19 April 2015. Orbits #1069 to #1073 illustrate the transition from a smooth topside profile to one of irregularities near and above ~240 km, to ionopause conditions and recovery. The largest depletions in $<TEC>_{topside}$ noted in Figure 6 come from heights ≥ 240 km. The LPW orbit segments correspond to the same orbit segments with simultaneous NGIMS data (as in Figure 6).

$<TEC>_{NGIMS}$ is ~12% lower than $<TEC>_{LPW}$. In Figure 6 (bottom), the averages of both instruments portray the "MAVEN $<TEC>_{topside}$" values, with the sample average being 4.98 ± 0.48 TECU. Clearly, both instruments and their averages show that 19 April had the lowest TEC values of the Deep-Dip-#2 campaign. The greatest differences occur for orbit #1071 with both instruments having values 1.0–1.4 TECU below their respective instrument means. For the two-instrument average values in Figure 6 (bottom), orbit #1071 shows an ~1.2 TECU decrease from its average value.

While this example from 19 April is the most severe ionopause event of the Deep-Dip-#2 campaign, many other orbits contained $N_e(h)$ gradient signatures attributed to ionopause crossings. These were described in *Mendillo et al.* [2015] using NGIMS observations only. Here we use 12 ionopause identifications (sharp topside gradients and/or transitions to $N_e < 10^3$ e$^-$/cm^3 below 300 km) seen simultaneously in both LPW and NGIMS data. These are indicated by the points in squares in Figure 6. The two-instrument averages for TEC depicted in Figure 6 (bottom) have 10 of the 12 TEC values below the sample mean, contributing to the large standard deviation. The two outliers result from $N_e(h)$ profiles with above average N_{max} values that produce large TEC values even though the topside ionosphere is depleted above ~300 km. Clearly, there is an extreme case of an ~1.2 TECU depletion, and more typical cases of ~0.4–0.6 TECU depletions associated with ionopause events. The implications of these magnitudes are discussed below.

The TEC depletion episode of 19 April 2015 is, not surprisingly, due to the transformation of the plasma density profile $N_e(h)$ from one with a smooth altitude gradient to one with a dramatic sharpening of that gradient—that is, to the appearance of an ionopause-like signature. This is shown in Figure 7 by using LPW data (note, in particular, the times associated with each orbit segment). Orbit #1069 inbound near 7:10 UT has a smooth gradient from the peak to ~300 km. One orbit later (#1070 inbound at ~11:40 UT) shows the onset of a turbulent pattern of multiple gradients. After periapse (10 min later, changing to #1071 outbound at ~11:50 UT), the LPW data reveal a dramatic solar wind-induced ionopause signature at ~240 km. Subsequent orbits #1072 and #1073 show a recovery pattern to smoother topside gradients. Thus, the depletion of topside TEC is due to the loss of plasma above ~240 km. Note that orbit #1072 is one of the outlier points in Figure 6, and thus associated with the recovery process.

While identifying ionopause-like signatures is relatively straight forward, finding the driving causes for steep density gradients is still a topic in need of study. For example, *Vogt et al.* [2015] offered several examples of factors associated with such events, and these ranged from observations of magnetic fields, ion and electron energy spectra, and changes in ion composition. They found that, on average, MAVEN's particles and field instruments showed that $N_e(h)$ profiles with an ionopause are accompanied by a higher energy flux of protons at high altitudes and stronger magnetic field at low altitude than for $N_e(h)$ patterns without an ionopause. Moreover, at ionospheric heights above ~300 km, the O^+/O_2^+ ratio was significantly larger for profiles with an ionopause versus those without one. Here we have used MAVEN's topside ionosphere profiles to characterize the changes in TEC associated with ionopause-like events. While beyond the scope of this paper, in a follow-up study we will relate TEC ionopause signatures to changes in solar wind parameters and associated reconfigurations of magnetic field topologies.

5.5. Speculation About Plasma Escape

How might TEC depletion episodes observed during MAVEN's Deep-Dip-#2 campaign be related to the far broader issues of plasma loss at Mars? The context for such studies started well prior to the MAVEN mission, with early results coming from the Russian Phobos-2 mission [*Lundin et al.*, 1989] and then many studies using ESA's Mars Express data sets [*Barabash et al.*, 2007; *Lundin et al.*, 2008, 2009; *Dubinin et al.*, 2009; *Fränz et al.*, 2010; *Nilsson et al.*, 2010, 2011; *Ramstad et al.*, 2013, and references therein]. The plasma escape rates found in all of these prior studies consistently fell within the range of ~10^{24} to ~10^{25} e^-/s. We now make estimates of the temporal changes in topside TEC due to ionopause episodes detected in MAVEN data with these previous vales of escape flux. To make an upper estimate, the ΔTEC value of 1.2 TECU for the largest depletion effect on 19 April 2015 (Figure 6, bottom) can be used. This change refers to local noon conditions, but from Figures 2 and 5 the TEC magnitudes change little during most daytime hours, except near dawn and dusk. For an upper limit we apply this value ($\Delta TEC = 1.2 \times 10^{15}$ ions/m^2) to the full daytime hemisphere. The dayside surface area at the height of the ionospheric peak (~130 km) is 7.8×10^{13} m^2. Thus, the total number of ion-electron pairs lost is 9.4×10^{28} for our maximum case. Given that the sampling rate is from one orbit to the next one (~4.5 h = 1.62×10^4 s), the change amounts to 5.8×10^{24} ions/s. This rough estimate is fully consistent with the range of 10^{24}–10^{25} ions/s from the Phobos-2 and MEX studies. The more typical ionopause signature of a TEC depletion shown in Figure 6 is about half that value, and thus, the escape flux would be 2.9×10^{24} ions/s. From MAVEN's own observations, the lower bound estimate for planetary escape of ions with energies >25 eV by *Brain et al.* [2015] was also ~3×10^{24} ions/s. The 25 eV ions observed beyond the ionosphere come, of course, from energized thermal ions previously in the ionosphere. *Jakosky et al.* [2015] used MAVEN observations and modeling to arrive at a rate of ~1.5×10^{24} ions/s for minimal solar wind conditions. Our finding here is that the routine loss of plasma from the ionosphere to the solar wind has detectable TEC signatures that result from relatively frequent ionopause events—occasionally enhanced by larger ones.

For long-term consequences, we can use the results above of ~13 ionopause events detected in 5 days. Ionopause detections of 2–3 per day are consistent with the finding that 54% of MAVEN's orbits exhibit an ionopause, most often at higher altitudes [*Vogt et al.*, 2015]. Using two events per day with the average TEC depletion ($\Delta TEC = 0.6 \times 10^{15}$ ions/m^2) and 365 earth days, total loss is 3.4×10^{31} ion-e^- pairs/year. Assuming O_2^+ to be the dominant ion feeding loss [*Vogt et al.*, 2015], the total ionospheric mass loss becomes 1.8×10^6 kg/yr. Over a three billion year span, this amounts to 5.4×10^{15} kg, approximately 20% of the mass of the current global Martian neutral atmosphere (~2.5×10^{16} kg).

6. Summary and Conclusions

We have investigated the use of observations of the Martian topside ionosphere made by instruments on the MAVEN spacecraft to characterize the reservoir of thermal plasma capable of escape. Prior to MAVEN's arrival at Mars, observations of the most robust regions of the Martian ionosphere—electron density profiles $N_e(h)$ near the subsolar point—were exceedingly sparse. Data obtained by MAVEN during its orbital Deep-Dip-#2 campaign (17–22 April 2015) provide an extraordinary opportunity to study the planet's maximum dayside plasma distributions on a day-to-day basis. We adopted the approach of using the parameter total electron content, defined as $TEC = \int N_e(h)dh$, to provide a consistent way to quantify overall cold plasma populations at Mars. MAVEN measured the contributions to TEC from plasma above the height of maximum electron density (from h_{max} to ~400 km), a height range that essentially coincided with the full topside ionosphere at Mars. Theoretical and climatological models of vertical electron density profiles were used to show that only small changes in topside shape and magnitude occur for the range of solar zenith angles (SZAs < 35°) encountered under midday conditions. This allowed us to integrate MAVEN's plasma data along its slanted orbital track (from ~400 km to the periapse height of ~132 km) as a reliable indicator of the vertical integral of $N_e(h)$ along the satellite track. We validated this concept by comparing the MAVEN-derived topside TEC with independent observations of full TEC made by the SHARAD instrument on MRO for 21 April 2015. Additional validation for the constancy of TEC under daytime conditions was achieved by integrating theoretical profiles from1-D and 3-D models of the Martian ionosphere. The day-to-day changes in the topside TEC from MAVEN can thus be interpreted as real changes in plasma content that can, potentially, be related to global escape fluxes. We offered approaches to that issue using rough calculations keyed to MAVEN data sets, showing that observed ionospheric plasma loss can be a significant component of overall atmospheric escape.

Acknowledgments

This work was supported, in part, by grants from the MAVEN Participating Scientist Program (NNX13AO20G for M. Mendillo and C. Narvaez) and the Mars Data Analysis Program (NNX15AM46G for M. Mendillo and C. Narvaez). M.F. Vogt acknowledges her support through NNX13AO35G (NASA grant from MAVEN Participating Scientist program to Paul Withers). F. Leblanc and J.Y. Chaufray are indebted to the program "Système Solaire" of CNES, the French space administration for its financial support on MAVEN. For this study we used MAVEN level 2 data: for NGIMS the sixth version (second revision) and for LPW the first version (fifth revision). These data are available to the public via the Planetary Plasma Interactions node of NASA's Planetary Data System at http://ppi.pds.nasa.gov/. The SHARAD/MRO data used are publicly accessible through the geosciences node of NASA's Planetary Data System at http://pds-geosciences.wustl.edu/. Finally, we are grateful to two reviewers who provided excellent comments and suggestions.

References

Andersson, L., et al. (2015), The Langmuir Probe and Waves (LPW) instrument for MAVEN, *Space Sci. Rev.*, *195*, 173, doi:10.1007/s11214-015-0194-3.

Barabash, S., A. Fedorov, R. Lundin, and J.-A. Sauvaud (2007), Martian atmospheric erosion rates, *Science*, *315*, 501–503, doi:10.1126/science.1134358.

Brain, D., et al. (2015), The spatial distribution of planetary ion fluxes near Mars observed by MAVEN, *Geophys. Res. Lett.*, *42*, 9142–9148, doi:10.1002/2015GL065293.

Campbell, B., and T. Watters (2016), Phase compensation of MARSIS subsurface sounding and estimation of ionospheric properties: New insights from SHARAD results, *J. Geophys. Res. Planets*, *121*, 180–193, doi:10.1002/2015JE004917.

Campbell, B., N. Putzig, L. Carter, and R. Phillips (2011), Autofocus correction of phase distortion effects on SHARAD echoes, *IEEE Geosci. Rem. Sensing Lett.*, *8*, 939–942, doi:10.1109/LGRS2011.2143692.

Campbell, B., N. Putzig, L. Carter, G. Morgan, R. Phillips, and J. Plaut (2013), Roughness and near-surface density of Mars from SHARAD radar echoes, *J. Geophys. Res. Planets*, *118*, 436–450, doi:10.1002/jgre.20050.

Campbell, B., N. Putzig, F. Foss II, and R. Phillips (2014), SHARAD signal attenuation and delay offsets due to the Martian ionosphere, *IEEE Geosci. Rem. Sensing Lett.*, *11*, 632–635, doi:10.1109/LGRS.2013.2273396.

Cartacci, M., et al. (2013), Mars ionosphere total electron content analysis from MARSIS subsurface data, *Icarus*, *223*, 423–437, doi:10.1016/j.icarus.2012.12.011.

Chaufray, J.-Y., F. Gonzalez-Galindo, F. Forget, M. Lopez-Valverde, F. Leblanc, R. Modolo, S. Hess, M. Yagi, P.-L. Blelly, and O. Witasse (2014), Three-dimensional Martian ionosphere model: II. Effect of transport processes due to pressure gradients, *J. Geophys. Res. Planets*, *119*, 1614–1636, doi:10.1002/2013JE004551.

Cui, J. M. G., R. Yelle, Y. Wei, and S.-J. Zhang (2015), Day-to-night transport in the Martian ionosphere: Implications from total electron content measurements, *J. Geophys. Res. Space Physics*, *120*, 2333–2346, doi:10.1002/2014JA020788.

Dubinin, E., M. Fraenz, J. Woch, S. Barabash, and R. Lundin (2009), Long-lived auroral structures and atmospheric losses through auroral flux tubes on Mars, *Geophys. Res. Lett.*, *36*, L08108, doi:10.1029/2009GL038209.

Duru, F., D. A. Gurnett, R. A. Frahm, J. D. Winningham, D. D. Morgan, and G. G. Howes (2009), Steep, transient density gradients in the Martian ionosphere similar to the ionopause at Venus, *J. Geophys. Res.*, *114*, A12310, doi:10.1029/2009JA014711.

Ergun, R. E., M. W. Morooka, L. A. Andersson, C. M. Fowler, G. T. Delory, D. J. Andrews, A. I. Eriksson, T. McEnulty, and B. M. Jakosky (2015), Dayside electron temperature and density profiles at Mars: First results from the MAVEN Langmuir probe and waves instrument, *Geophys. Res. Lett.*, *42*, 8846–8853, doi:10.1002/2015GL065280.

Forget, F., F. Hourdin, R. Fournier, C. Hourdin, and O. Talagrand (1999), Improved general circulation models of the Martian atmosphere from the surface to above 80 km, *J. Geophys. Res.*, *104*, 24,155–24,175, doi:10.1029/1999JE001025.

Fox, J. L. (2004), Response of the Martian thermosphere/ionosphere to enhanced fluxes of solar soft X rays, *J. Geophys. Res.*, *109*, A11310, doi:10.1029/2004JA010380.

Fränz, M., E. Dubinin, E. Nielsen, J. Woch, S. Barabash, R. Lundin, and A. Fedorov (2010), Transterminator ion flow in the Martian ionosphere, *Planet. Space Sci.*, *58*, 1442–1454, doi:10.1016/j.pss.2010.06.009.

Gonzalez-Galindo, F., J.-Y. Chaufray, M. A. Lopez-Valverde, G. Gilli, F. Forget, F. Leblanc, R. Modolo, S. Hess, and M. Yagi (2013), Three-dimensional Martian ionosphere model: I The photochemical ionosphere below 180 km, *J. Geophys. Res. Planets*, *118*, 2105–2123, doi:10.1002/jgre.20150.

Haider, S., K. Mahajan, and E. Kallio (2011), Mars ionosphere: A review of experimental results and modeling studies, *Rev. Geophys.*, *49*, RG4001, doi:10.1029/2011RG000357.

Hinson, D., R. Simpson, J. Twicken, G. Tyler, and F. Flasar (1999), Initial results from the radio occultation measurements with Mars Global Surveyor, *J. Geophys. Res.*, *104*, 26,997–27,012, doi:10.1029/1999JE001069.

Jakosky, B. (2015), MAVEN explores the Martian upper atmosphere, *Science*, *350*, 643, doi:10.1126/science.aad3443.

Jakosky, B., et al. (2015), MAVEN observations of the response of Mars to an interplanetary coronal mass ejection, *Science*, *350*(6261), doi:10.1126/science.aad0210.

Jordan, R., et al. (2009), The Mars Express MARSIS sounder instrument, *Planet. Space Sci.*, *57*, 1975–1986, doi:10.1016/j.pss.2009.09.016.

Lillis, R., D. Brain, S. England, P. Withers, M. Fillingim, and A. Safaeinili (2010), Total electron content in the Mars ionosphere: Temporal studies and dependence on solar EUV flux, *J. Geophys. Res.*, *115*, A11314, doi:10.1029/2010JA01598.

Lundin, R., B. Hultqvist, S. Olsen, R. Pellinen, I. Liede, A. Zakharov, E. Dubinin, and N. Pissarenko (1989), The ASPERA experiment on the Soviet Phobos spacecraft, in *Solar System Plasma Physics, Geophys. Monogr. Ser.*, vol. 54, edited by J. H. Waite Jr., J. L. Burch, and R. L. Moore, pp. 417–424, AGU, Washington, D. C., doi:10.1029/GM054p0417.

Lundin, R., S. Barabash, A. Fedorov, M. Holmström, H. Nilsson, J.-A. Sauvaud, and M. Yamauchi (2008), Solar forcing and planetary ion escape from Mars, *Geophys. Res. Lett.*, *35*, L09203, doi:10.1029/2007GL032884.

Lundin, R., S. Barabash, M. Holmström, H. Nilsson, M. Yamauchi, E. M. Dubinin, and M. Fraenz (2009), Atmospheric origin of cold ion escape from Mars, *Geophys. Res. Lett.*, *36*, L17202, doi:10.1029/2009GL039341.

Ma, Y., A. Nagy, I. Sokolov, and K. Hansen (2004), Three-dimensional, multispecies, high spatial resolution MHD studies of the solar wind interaction with Mars, *J. Geophys. Res.*, *109*, A07211, doi:10.1019/2003JA010367.

Mahaffy, P., et al. (2014), The neutral gas and ion mass spectrometer on the Mars atmosphere and volatile evolution mission, *Space Sci. Rev.*, *195*, 49, doi:10.1007/s11214-014-0091-1.

Martinis, C. R., J. Wilson, and M. Mendillo (2003), Modeling day-to-day ionospheric variability on Mars, *J. Geophys. Res.*, *108*, 1383, doi:10.1029/2003JA009973.

Mayyasi, M., and M. Mendillo (2015), Why the Viking descent probes found only one ionospheric layer at Mars, *Geophys. Res. Lett.*, *42*, 7359–7365, doi:10.1002/2015GL065575.

Mendillo, M., X. Pi, S. Smith, C. Martinis, J. Wilson, and D. Hinson (2004), Ionospheric effects upon a satellite navigation system at Mars, *Radio Sci.*, *39*, RS2028, doi:10.1029/2003RS002933.

Mendillo, M., A. Lollo, P. Withers, M. Patzold, and S. Tellmann (2011), Modeling Mars' ionosphere with contraints from same-day observations by Mars Global and Mars Express, *J. Geophys.*, *116*, A11303, doi:10.1029/2011JA016865.

Mendillo, M., A. Marusiak, P. Withers, D. Morgan, and D. Gurnett (2013a), A new semi-empirical model of the peak electron density of the Martian ionosphere, *Geophys. Res. Lett.*, *40*, 5361–5165, doi:10.1002/2013GL057631.

Mendillo, M., C. Narvaez, P. Withers, M. Matta, W. Kofman, and J. Mouginot (2013b), Variability in ionospheric total electron content at Mars, *Planet. Space Sci.*, *86*, 117–129, doi:10.1016/j.pss.2013.08.010.

Mendillo, M., C. Narvaez, M. Matta, M. Vogt, P. Mahaffy, M. Benna, and B. Jakosky (2015), MAVEN and the Mars Initial Reference Ionosphere model, *Geophys. Res. Lett.*, *42*, 9080–9086, doi:10.1002/2015GL065732.

Mouginot, J., W. Kofman, A. Safaeinili, and A. Herique (2008), Correction of the ionospheric distortion on the MARSIS surface sounding echoes, *Planet. Space Sci.*, *56*, 917–56,926, doi:10.1016/j.pss.2008.01.010.

Němec, F., D. Morgan, D. Gurnett, F. Duru, and V. Truhlík (2011), Dayside ionosphere of Mars: Empirical model based on data from the MARSIS instrument, *J. Geophys. Res.*, *116*, doi:10.1029/2010JE003789.

Němec, F., D. Morgan, D. Gurnett, and D. Andrews (2016), Empirical model of the Martian dayside ionosphere: Effects of crustal magnetic fields and solar ionizing flux at higher altitudes, *J. Geophys. Res. Space Physics*, *121*, 1760–1771, doi:10.1002/2015/A022060.

Nilsson, H., E. Carlsson, D. Brain, M. Yamauchi, M. Holmström, S. Barabash, R. Lundin, and Y. Futaana (2010), Ion escape from Mars as a function of solar wind conditions: A statistical study, *Icarus*, *206*, 2010, doi:10.1016/j.icarus.2009.03.006.

Nilsson, H., et al. (2011), Heavy ion escape from Mars, influence from solar wind conditions and crustal magnetic fields, *Icarus*, *215*, 475–484, doi:10.1016/j.icarus.2011.08.003.

Picardi, G., et al. (2004), Performance and surface scattering models for the Mars advanced radar for subsurface and ionospheric sounding (MARSIS), *Planet. Space Sci.*, *52*, 149–156, doi:10.1016/j.pss.2003.08.020.

Picardi, G., et al. (2005), Radar soundings of the subsurface of Mars, *Science*, *310*, 1925–1928, doi:10.1126/science.1122165.

Ramstad, R., Y. Futaana, S. Barabash, H. Nilsson, S. M. del Campo B, R. Lundin, and K. Schwingenschuh (2013), Phobos 2/ASPERA data revisited: Planetary ion escape rate from Mars near the 1989 solar maximum, *Geophys. Res. Lett.*, *40*, 477–481, doi:10.1002/grl.50149.

Ratcliffe, J. (1960), *Physics of the Upper Atmosphere*, Academic Press, New York.

Rishbeth, H., and O. Garriot (1969), *Introduction to Ionospheric Physics*, Academic Press, New York.

Safaeinili, A., W. Kofman, J. Nouvel, A. Herique, and R. Jordan (2003), Impact of Mars ionosphere on orbital radar sounder operation and data processing, *Planet. Space Sci.*, *51*, 505–515, doi:10.1016/S0032-0633(03)00048-5.

Safaeinili, A., et al. (2007), Estimation of the total electron content of the Martian ionosphere using radar sounder surface echoes, *Geophys. Res. Lett.*, *34*, L23204, doi:10.1029/2007GL032154.

Sanchez-Cano, B., et al. (2015), Total electron content in the Martian atmosphere: A critical reassessment of the Mars Express MARSIS data sets, *J. Geophys. Res. Space Physics*, *120*, 2166–2182, doi:10.1002/2014JA020630.

Seu, R., et al. (2007), The SHARAD sounding radar on MRO, *J. Geophys. Res.*, *112*, E05S05, doi:10.1029/2006JE002475.

Vogt, M. F., et al. (2015), Ionopause-like density gradients in the Martian ionosphere: A first look with MAVEN, *Geophys. Res. Lett.*, *42*, 8885–8893, doi:10.1002/2015GL065269.

Withers, P. (2009), A review of observed variability in the dayside ionosphere of Mars, *Adv. Space Res.*, *44*, 277–307, doi:10.1016/j.asr.2009.04.027.

Withers, P., et al. (2012), Observations of the nightside ionosphere of Mars by the Mars Radio Science Experiment (MaRS), *J. Geophys. Res.*, *117*, A12307, doi:10.1029/2012JA018185.

Zhang, Z., E. Nielsen, J. Plaut, R. Orosei, and G. Picardi (2009), Ionospheric corrections of MARSIS subsurface sounding signals with filters including collision frequency, *Planet. Space Sci.*, *57*(2009), 393–403, doi:10.1016/j.pss.2008.11.016.